ACS APPLIED ENERGY MATERIALS

www.acsaem.org Article

# Ultrafine Sb Pillared Few-Layered $Ti_3C_2T_x$ MXenes for Advanced Sodium Storage

Shunlong Zhang,[§] Hangjun Ying,[§] Pengfei Huang, Jianli Wang, Zhao Zhang, Zhihao Zhang, and Wei-Qiang Han*

Cite This: *ACS Appl. Energy Mater.* 2021, 4, 9806−9815 Read Online

ACCESS | Metrics & More | Article Recommendations | Supporting Information



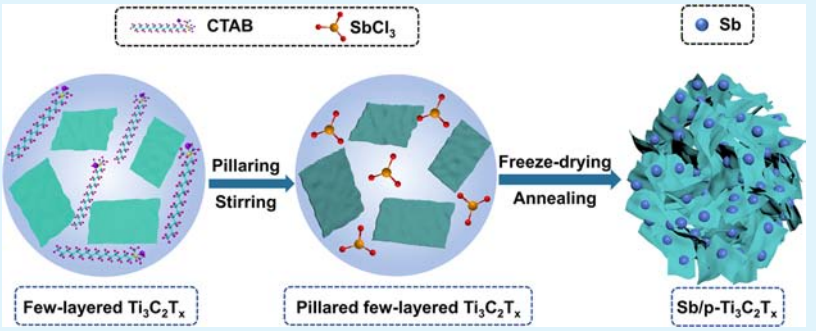


**ABSTRACT:** Pillaring technology has proven to be an effective strategy to improve the electrochemical performance of MXene-based composites, especially the rate performance due to the enlarged interlayer spacing. Taking the larger radius of sodium ions into account, it is urgent to develop pillared MXene-based composites for sodium-ion batteries (SIBs). To fully deliver high rate performance of pillared MXenes and high capacity of Sb in SIBs, in this work, we exquisitely decorate ultrafine Sb particles onto flexible few-layered $Ti_3C_2T_x$ (f-$Ti_3C_2T_x$) nanosheets to fabricate Sb pillared $Ti_3C_2T_x$ (Sb/p-$Ti_3C_2T_x$) composites through facile electrostatic adsorption followed by the annealing process. Benefiting from the enhanced kinetics properties by highly conductive pillared f-$Ti_3C_2T_x$ and ultrafine Sb nanoparticles, the composites exhibit a reversible charge capacity of 438.1 mAh $g^{-1}$ at 50 mA $g^{-1}$ and a high retention rate of 126.6 mAh $g^{-1}$ at 2 A $g^{-1}$. Furthermore, the strong interaction between Sb and $Ti_3C_2T_x$ via Ti−O−Sb chemical bonding endows the composites with high structural stability, leading to good cycling sustainability. More importantly, for the first time, we succeed in integrating dual advantages of the few-layered state of MXenes and pillaring technology in MXene-based composites for SIBs. This work supplies an effective modification strategy to conquer the drawbacks of Sb anodes and achieve exploitation of pillared few-layered MXene composites in SIBs, promoting the commercial process of MXenes in SIBs.

**KEYWORDS:** *few-layered MXenes, pillared MXenes, $Ti_3C_2T_x$, ultrafine Sb, sodium-ion storage*

## INTRODUCTION

MXenes are first discovered in 2011[1−4] and have developed explosively in recent years because of their novel structure and characteristics,[5−8] leading to a wide range of applications,[9−12] together with more varieties of MXenes (Figure S1).[13,14] $Ti_3C_2T_x$ ($T_x$ denotes the surface terminal groups, typically −O, −OH, and −F) is one of the most extensively studied MXenes with outstanding advantages including high metallic conductivity, adjustable interlayer spacing, and low diffusion barrier for alkali metal ions.[15−17] Due to challenges of energy and environment,[18,19] these merits enable $Ti_3C_2T_x$ as an ideal candidate in energy storage systems of sodium-ion batteries (SIBs),[20] which have been regarded as one of the most competitive alternatives to lithium-ion batteries (LIBs) because of their advantages of abundant sodium reserves, low price, and comparable performance.[21,22] However, the larger ionic radius and heavier atomic weight of Na lead to more sluggish kinetics,[23,24] larger volume expansion, and lower specific capacity.[25] Therefore, seeking suitable anodes for SIBs than those for LIBs is a greater challenge.[26]

To date, some previous works have confirmed the availability of $Ti_3C_2T_x$ in SIBs.[27−30] However, the current performance of $Ti_3C_2T_x$ in SIBs is still deficient because of severe aggregation of MXene nanosheets, adverse effects of surface functional groups, and inadequate interlayer spacing.[31−33] Fortunately, decreasing the number of $Ti_3C_2T_x$ layers and enlarging the interlayer spacing via pillaring technology are

**Received:** June 28, 2021
**Accepted:** August 12, 2021
**Published:** August 25, 2021

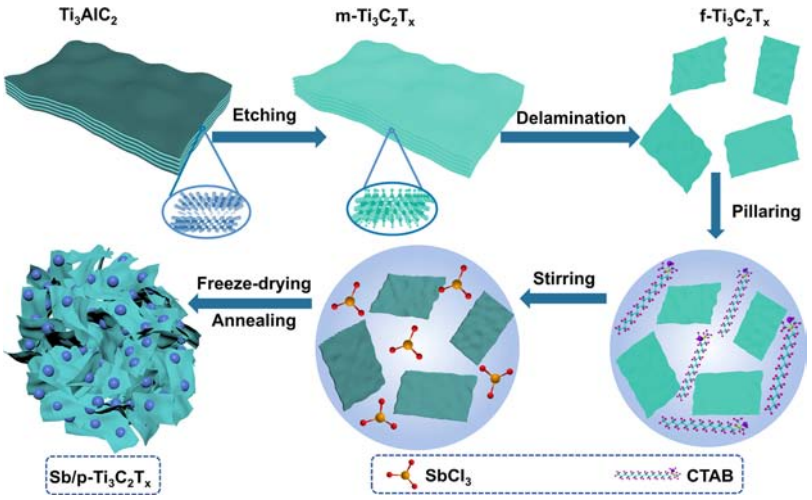


**Figure 1.** Schematic preparation of f-$Ti_3C_2T_x$ MXenes and subsequent Sb/p-$Ti_3C_2T_x$ composites.

proven effective means to improve the electrochemical performance of MXenes.[6,34] For instance, Zhang et al. synthesized f-$Ti_3C_2T_x$ through organic solvent-assistant high energy ball milling and proved that delaminated f-$Ti_3C_2T_x$ can deliver 267 mAh $g^{-1}$ at 0.1 A $g^{-1}$ in SIBs, more than twice the value of pristine MXene.[35] Tao et al. demonstrated the excellent storage capability of $Ti_3C_2$ with an expanded interlayer spacing via the pillaring method. The atomic S-intercalated $Ti_3C_2$ (CT-S@$Ti_3C_2$) electrode exhibits enhanced sodium ability with 550 mAh $g^{-1}$ at 0.1 A $g^{-1}$, in contrast to only 98 mAh $g^{-1}$ for $T_3C_2$.[25] However, most of these MXene-based composites were at the multilayered state or assisted by carbon materials, such as CNTs or graphene, making the function of MXenes unclear. Besides, there are still various major challenges in MXenes.[30,36,37]

Among anode candidates of SIBs, Sb has attracted great interest because of its high theoretical specific capacity and moderate operation voltage (0.5−0.8 V vs $Na/Na^+$).[38] However, the drastic volume change during sodiation/desodiation (~290%) results in poor cycle sustainability, and insufficient conductivity leads to unfavorable rate performance.[39] Considering the distinguished properties of MXenes,[40−42] MXenes can be used as substrates to simultaneously buffer the volume fluctuation, inhibit particle aggregation, and improve the kinetics.[43] Especially, there is no report about pillared few-layered MXene (f-MXene) composites for anodes in SIBs, integrating dual advantages of the few-layered state and pillaring technology with larger interlayer spacings. Exploring the preparation of Sb pillared MXenes is of great significance to promote the development of pillared MXenes in SIBs, broadening the preparation and application of pillared MXenes from LIBs to SIBs.[44,45]

Recently, our group developed a solution-phase flocculation process to fast prepare few-layered MXene nanosheets.[45−47] The as-synthesized f-$Ti_3C_2T_x$ nanosheets show a flexible morphology with ample surface and interlamellar space, can be used as an ideal matrix for SIB anodes. Herein, we elaborately designed Sb pillared $Ti_3C_2T_x$ (Sb/p-$Ti_3C_2T_x$) composites, together with ultrafine Sb particles tightly decorated onto f-$Ti_3C_2T_x$. The expanded interlayer space of f-$Ti_3C_2T_x$ and ultrafine Sb particles can effectively shorten the ion diffusion distance and supply mighty storage ability for $Na^+$. Moreover, the synergistic effect between the f-$Ti_3C_2T_x$ matrix and Sb nanoparticles can optimize the electrochemical performance of each other. On the one hand, the highly conductive MXene nanosheets with abundant active sites and inner space not only adequately buffer the volume fluctuation and inhibit the aggregation of Sb particles but also boost electronic transport. On the other hand, the ultrafine Sb particles work as a barrier to effectively restrain the restacking of $Ti_3C_2T_x$ nanosheets and stabilize the interlayer spacings. Benefiting from the ingenious design, the Sb/p-$Ti_3C_2T_x$ composites exhibit excellent ability in sodium storage.

## EXPERIMENTAL SECTION

**Preparation of Multilayered $Ti_3C_2T_x$.** $Ti_3AlC_2$ MAX (98%, 200 mesh) was [redacted]. Accordion-like multilayered $Ti_3C_2T_x$ (m-$Ti_3C_2T_x$) can be prepared according to the previous report.[46]

**Preparation of Few-Layered $Ti_3C_2T_x$.** Few-layered $Ti_3C_2T_x$ (f-$Ti_3C_2T_x$) can be fast prepared based on our group's recently reported step-by-step delamination strategy and the modified solution-phase flocculation (MSPF) method, which can effectively avoid the formation of fragments and increase the yield of f-$Ti_3C_2T_x$, together with the fundamental settlement of the restacking phenomenon of f-$Ti_3C_2T_x$.[46,48]

**Preparation of Sb/p-$Ti_3C_2T_x$ MXene Composites.** f-$Ti_3C_2T_x$ was first prepillared by hexadecyltrimethylammonium bromide (CTAB) to enlarge the interlayer spacing in CTAB solutions. In detail, 190 mg of f-$Ti_3C_2T_x$ was immersed into 120 mL of a 0.2 wt % CTAB solution for achieving prepillaring with stirring (35 °C, 24 h). After that, 500 mg of $SbCl_3$ was added to complete the ion-exchange process and adsorption of $Sb^{3+}$ on the surface of $Ti_3C_2T_x$. Thirty milliliters of 1 M HCl was also added into the solution to avoid the hydrolysis of $Sb^{3+}$. After subsequent centrifugation, washing with 0.1 M HCl, freeze-drying, and the annealing process (180 °C, 2 h, Ar atmosphere), the final 293 mg of Sb/p-$Ti_3C_2T_x$ composites can be obtained. The same process can also be carried out for the preparation of Sb/$Ti_3C_2T_x$ composites except for the CTAB prepillaring process.

**Material Characterization.** Traditional measurements were performed according to the previous report,[45] including X-ray diffraction (XRD), scanning electron microscopy (SEM), transmission electron microscopy (TEM), X-ray photoelectron spectroscopy (XPS), and Brunauer−Emmett−Teller (BET) surface area.

**Electrochemical Measurements.** The samples were evaluated by assembling 2032 coin cells. The working electrode was composed of active materials, acetylene black, and a CMC binder in a weight ratio of 70:15:15. Sodium metal discs were used as the counter electrode. Glass fiber (Whatman, GF/D) was used as the separator,


https://doi.org/10.1021/acsaem.1c01863
ACS Appl. Energy Mater. 2021, 4, 9806−9815

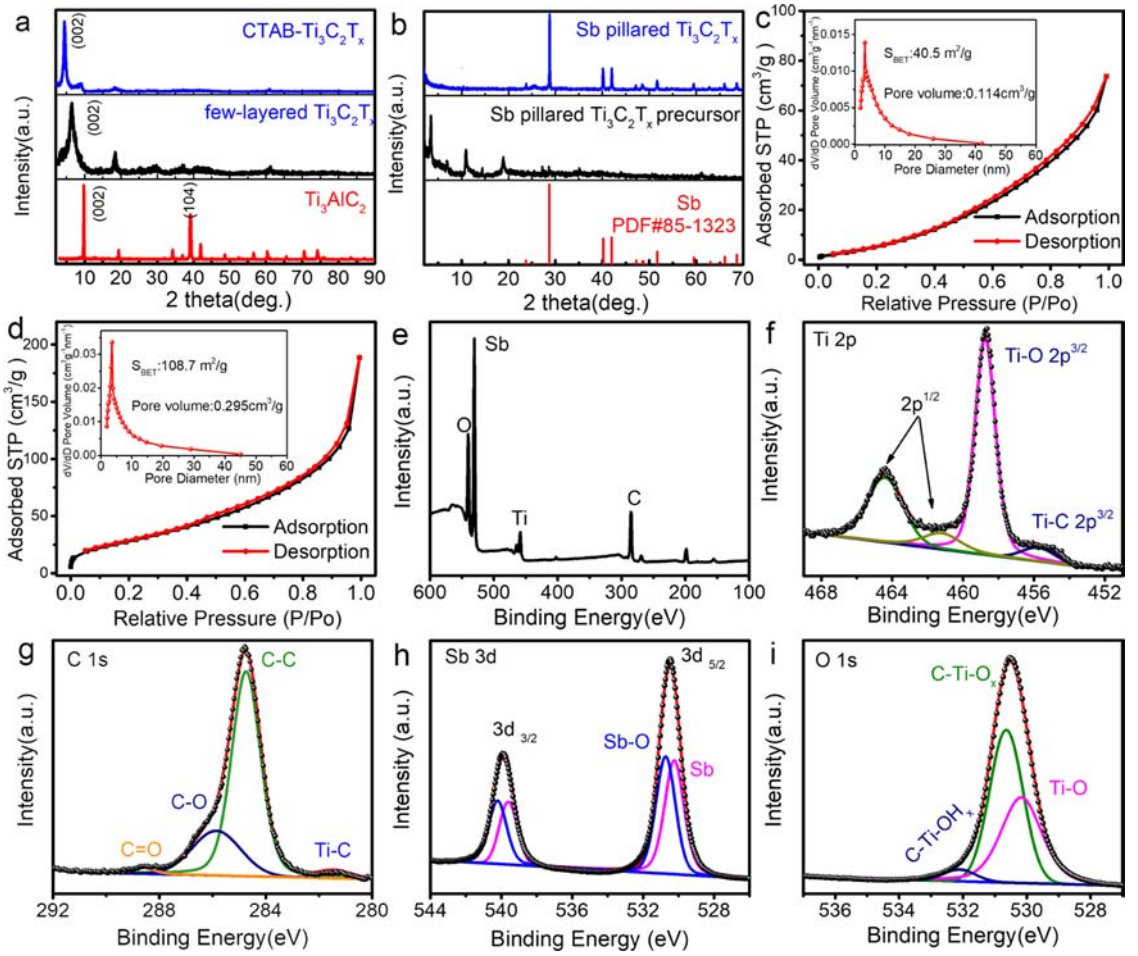


**Figure 2.** (a, b) XRD patterns of related materials. (c, d) $N_2$ adsorption/desorption and pore size distribution of f-$Ti_3C_2T_x$ and Sb/p-$Ti_3C_2T_x$ composites. (e–i) XPS spectra of Sb/p-$Ti_3C_2T_x$ composites for the full spectrum, Ti 2p, C 1s, Sb 3d, and O 1s, respectively.

and 1 M $NaClO_4$ in EC:PC (1:1 v/v) with 5% fluoroethylene carbonate (FEC) was used as the electrolyte.

## RESULTS AND DISCUSSION

The synthesis processes of f-$Ti_3C_2T_x$ and Sb/p-$Ti_3C_2T_x$ composites are schematically described in Figure 1. Originally, accordion-like m-$Ti_3C_2T_x$ can be synthesized through etching away the Al layer in the $Ti_3AlC_2$ MAX phase.[46,49−52] Afterward, the lamellar-like few-layered or even single-layered $Ti_3C_2T_x$ nanosheets were obtained by step-by-step ultrasonic delamination in water. To rapidly collect the product and inhibit the restacking phenomenon, we originally employed solution-phase flocculation with the assistance of ammonium salts, which can be easily volatilized via subsequent heat treatment. The step-by-step delamination combined with solution-phase flocculation technology could greatly improve the yield and production efficiency of f-MXenes from multilayered MXenes. To further prepare Sb/p-$Ti_3C_2T_x$ composites, we first enlarged the interlayer spacing of $Ti_3C_2T_x$ by hexadecyltrimethylammonium bromide (CTAB) prepillaring. The subsequently added $Sb^{3+}$ in the form of $SbCl_3$ was readily inserted into the $Ti_3C_2T_x$ interlayer through the ion-exchange process or adhered to the surface via interactions between $Sb^{3+}$ (positively) and f-$Ti_3C_2T_x$ (negatively) due to the electrostatic attraction,[53] leading to the formation of flocculation. After freeze-drying and annealing processes, the residual CTAB was volatilized, and the antimony precursor was reduced to metallic Sb nanoparticles, thereby obtaining Sb pillared f-$Ti_3C_2T_x$ composites.

The structural evolution process of related materials can be lucidly presented by the XRD test. As shown in Figure 2a, the raw material reveals typical diffraction peaks corresponding to the $Ti_3AlC_2$ MAX phase. After HF etching, the following remarkable changes can be observed in the XRD pattern: the peak (104) at 39° disappears and the peak (002) shifts to the left, indicating the successful removal of the Al layer and the enlargement of the interlayer spacing along the lattice plane (002).[54] CTAB prepillaring further makes a left shift of the peak (002), testifying the further expansion of the (002) plane with the intercalation of long-chain CTAB molecules.[55] The precursor of Sb pillared $Ti_3C_2T_x$ does not exhibit any diffraction peaks corresponding to Sb-related phases, suggesting the amorphous state of the precursor of Sb. After the annealing process, the precursor of Sb is successfully converted to metallic Sb (PDF # 85-1323; Figure 2b). Particularly, during the annealing process, Sb clusters were formed due to the aggregation of partially intercalated atomic Sb,[47] leading to further increase of the interlayer spacing and reduction of the degree of ordering of $Ti_3C_2T_x$. Therefore, the (002) peak of $Ti_3C_2T_x$ is nearly invisible.[56] The result also indicates the effective suppression of the self-restacking of $Ti_3C_2T_x$. Although possessing a two-dimensional layered structure, f-$Ti_3C_2T_x$ displays a moderate specific surface area of 40.5 $m^2$ $g^{-1}$ according to the isothermal $N_2$ adsorption/desorption


https://doi.org/10.1021/acsaem.1c01863
ACS Appl. Energy Mater. 2021, 4, 9806−9815

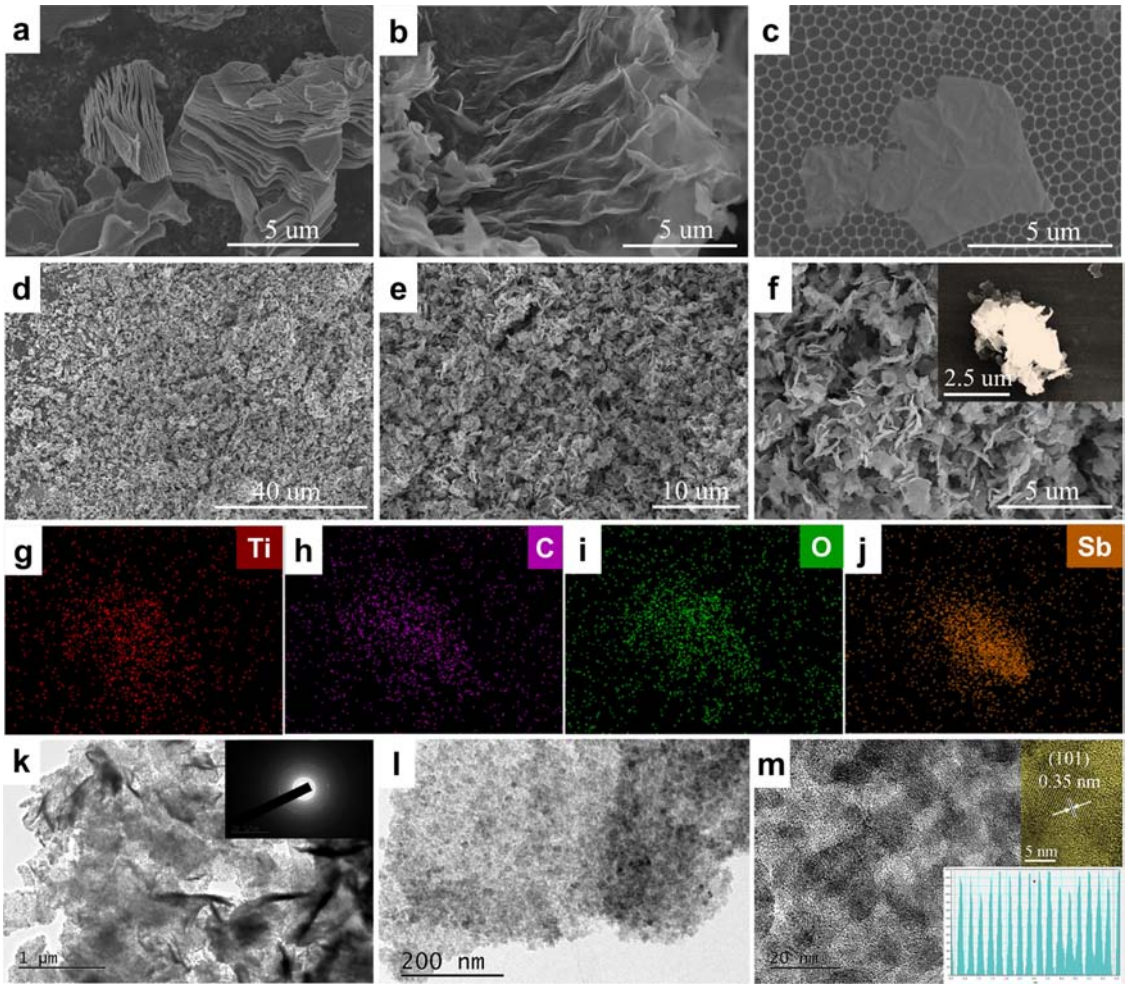


**Figure 3.** (a) SEM images of accordion-like m-$Ti_3C_2T_x$. (b) SEM images of f-$Ti_3C_2T_x$ powders. (c) SEM image of f-$Ti_3C_2T_x$ on the AAO film. (d–f) SEM images of Sb/p-$Ti_3C_2T_x$ composites. (g–j) Corresponding elemental mapping of Ti, C, O, and Sb based on the inset in (f). (k–m) TEM and HRTEM of Sb/p-$Ti_3C_2T_x$ composites.

curve (Figure 2c), in contrast to the extremely high specific surface area usually obtained in graphene with similar morphology.[57] The relatively flawless surface could provide sufficient sites for loading Sb nanoparticles and effectively inhibit the irreversible insertion of $Na^+$ in the defects. After decoration of Sb nanoparticles, the specific surface area increases significantly to 108.7 $m^2\ g^{-1}$, and the pore volume improves to 0.295 $cm^3\ g^{-1}$ compared to 0.144 $cm^3\ g^{-1}$ for bare f-$Ti_3C_2T_x$ (Figure 2d). The increased specific surface area mainly comes from ultrafine Sb particles, which could provide abundant active sites, beneficial to the rapid access of $Na^+$.

As shown in Figure 3, the morphological information of the materials is collected by scanning electron microscopy (SEM) and transmission electron microscopy (TEM). Compared with compact raw $Ti_3AlC_2$ MAX bulks (Figure S2), the as-synthesized m-$Ti_3C_2T_x$ MXenes exhibit an obvious accordion-like morphology (Figures 3a and S3). After the delamination process, the f-$Ti_3C_2T_x$ MXenes can be obtained with a lamina-like morphology, and slight wrinkles can be observed at the surface (Figure 3b,c). According to previous work, the thickness of the as-synthesized ultrathin MXenes is about several layers (typically 2–3 layers) or even a single layer.[46] As SEM images at different magnifications shown in Figure 3d–f, after compositing with Sb nanoparticles, $Ti_3C_2T_x$ still retains the lamellar structure except for the obvious increase of the thickness due to partial intercalated Sb. The homogeneous decoration of Sb can be intuitively presented by EDS elemental mapping, in which the distributions of Ti, C, Sb, and O well match the morphology of the composites (the inset of Figure 3f,g–j), together with a Sb content of 39.55 wt % (Figure S4). More detailed features of Sb/p-$Ti_3C_2T_x$ composites are recorded by TEM. The uniform distribution of ultrafine Sb particles on the $Ti_3C_2T_x$ nanosheets can be further confirmed in Figure 3k,l; moreover, no aggregation of Sb nanoparticles occurs at the MXene matrix (Figure 3l). The selected area electron diffraction (SAED) pattern reveals the polycrystalline state of Sb nanoparticles and $Ti_3C_2T_x$ (the inset of Figure 3k). High-resolution transmission electron microscopy (HRTEM) shows that monodispersed Sb nanoparticles around 10 nm are evenly embedded in the conductive $Ti_3C_2T_x$ matrix. Accurate measurement reveals a d-spacing of 0.35 nm, corresponding to the (101) plane of metallic Sb. Compared with pure Sb powders (Figures S5 and S6), Sb/p-$Ti_3C_2T_x$ combines the advantages of the high capacity of Sb and a large interlayer spacing of $Ti_3C_2T_x$, showing the potential application in SIBs.

As demonstrated by the structure and morphology characterizations, f-$Ti_3C_2T_x$ nanosheets are ideal matrices for stowing Sb nanoparticles, mainly due to the positive affinity interaction between the precursor metallic cation and the


https://doi.org/10.1021/acsaem.1c01863
ACS Appl. Energy Mater. 2021, 4, 9806–9815

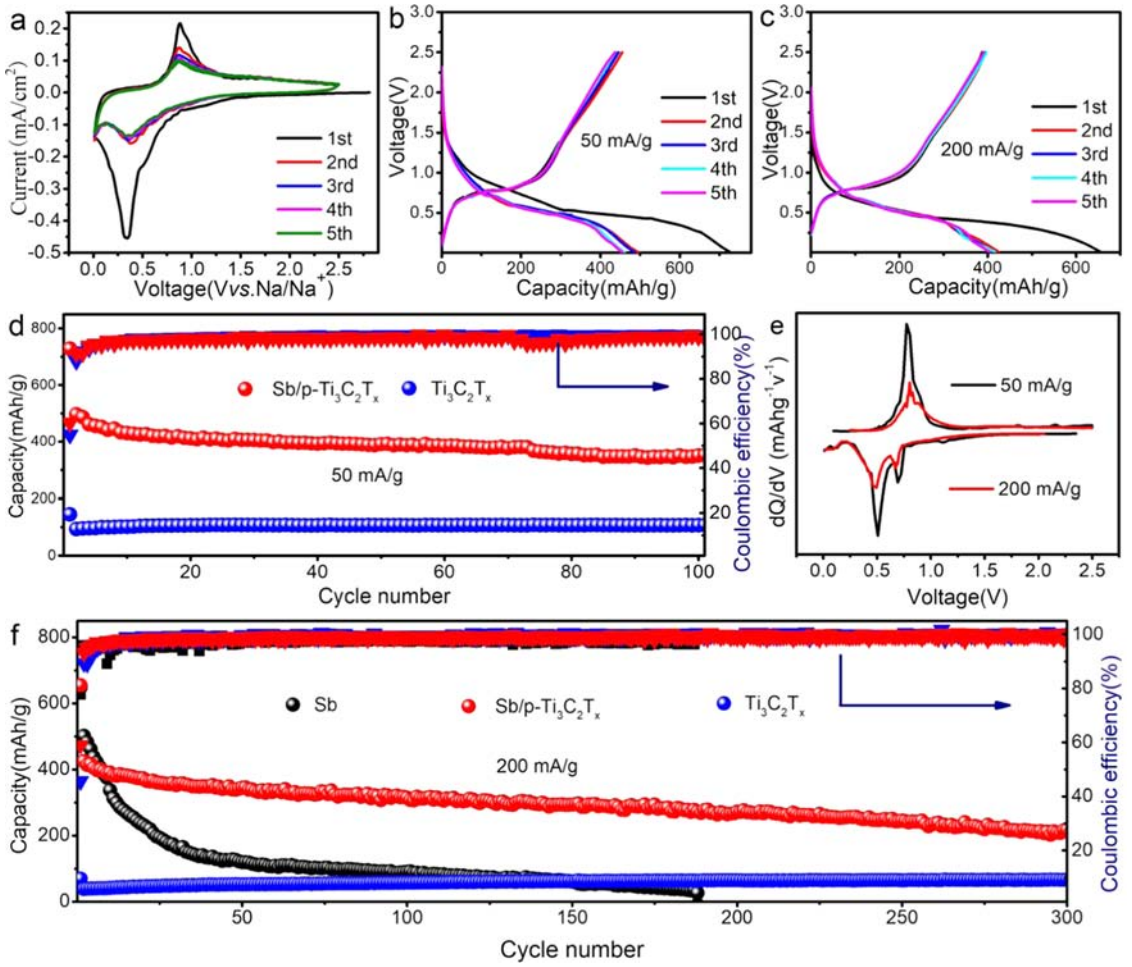


**Figure 4.** (a) CV curves of Sb/p-$Ti_3C_2T_x$ composites. (b, c) Typical discharge/charge profiles of Sb/p-$Ti_3C_2T_x$ composites at 50 and 200 mA $g^{-1}$, respectively. (d) Cycling performance of $Ti_3C_2T_x$ and Sb/p-$Ti_3C_2T_x$ composites at 50 mA $g^{-1}$. (e) Differential capacity versus voltage curve in the fifth cycle at different current densities. (f) Cycling performance of $Ti_3C_2T_x$ and Sb/p-$Ti_3C_2T_x$ composites at 200 mA $g^{-1}$.

surface groups of $Ti_3C_2T_x$ nanosheets.[32,58] X-ray photoelectron spectroscopy (XPS) is carried out to study the surface chemical properties (Figure 2e–i). As displayed in Figure 2e, signals of O, Sb, Ti, and C can be detected in the XPS full spectrum. Because XPS is a surface characterization technique with a detection depth of several nanometers, an extremely strong Sb peak implies the uniform coverage of Sb nanoparticles on the $Ti_3C_2T_x$ nanosheets, consistent with the above discussion. The Ti 2p spectrum can be divided into Ti $2p_{1/2}$ with higher binding energy and Ti $2p_{3/2}$ with lower binding energy, which can be further deconvoluted into two doublets. The peaks at 458.7 and 455.6 eV are attributed to Ti–O $2p_{3/2}$ and Ti–C $2p_{3/2}$, respectively (Figure 2f).[59] The C 1s spectrum can be deconvoluted into four peaks, corresponding to C=O (288.6 eV), C–O (286.0 eV), C–C (284.8 eV), and Ti–C (281.4 eV) bonds (Figure 2g).[58] The Sb 3d spectrum consists of Sb $3d_{3/2}$ and Sb $3d_{5/2}$, which can be further divided into two doublets, and two peaks with higher binding energy belongs to Sb–O chemical bonds, while the relatively weak peaks at 539.5 and 530.2 eV are correlated to $Sb^0$ (Figure 2h).[60] The surface Sb atoms are inevitably oxidized when interact with oxygen-containing groups absorbed by $Ti_3C_2T_x$, consistent with previous reports.[58,61] In addition, the O 1s of Sb/p-$Ti_3C_2T_x$ composites generates peaks at 532.2, 530.6, and 530.14 eV, which can be assigned to Ti–$OH_x$, Ti–$O_x$–Sb, and Ti–O, respectively, revealing the abundant surface oxygen-containing groups (Figure 2i).[62,63] According to the XPS analysis, strong affinity interactions could form between Sb nanoparticles and f-$Ti_3C_2T_x$ through an interfacial "oxygen bridge", such as Ti–O–Sb.[58,64,65] The affinity based on electrostatic attraction and chemical bonding plays an important role in the formation of microstructures and further influences the electrochemical performance of the composites. The affinity force strongly attracts the Sb precursor and anchors nano-Sb, thereby inhibiting the aggregation and coarsening of the particles. Moreover, the tight anchoring of the Sb nanoparticles grants the robustness of the composites and assures excellent electrochemical performance.

The electrochemical sodium storage performance is evaluated by 2032-type coin cells using a sodium metal foil as the counter electrode. As shown in Figure 4a, the electrochemical mechanism of Sb/p-$Ti_3C_2T_x$ is studied using the cyclic voltammetry (CV) test. In the cathodic scan, a broad hump ranging from 0.90 to 1.43 V observed in the initial cycle but disappeared in the following cycles can be ascribed to the irreversible side reactions, e.g., the formation of a solid–electrolyte interface (SEI) membrane.[66,67] Similar irreversible loss of capacity can also be observed in pure Sb nanoparticles (Figure S7). The following overlapping fluctuations centered at around 0.57 and 0.34 V are attributed to the multistep


https://doi.org/10.1021/acsaem.1c01863
ACS Appl. Energy Mater. 2021, 4, 9806–9815

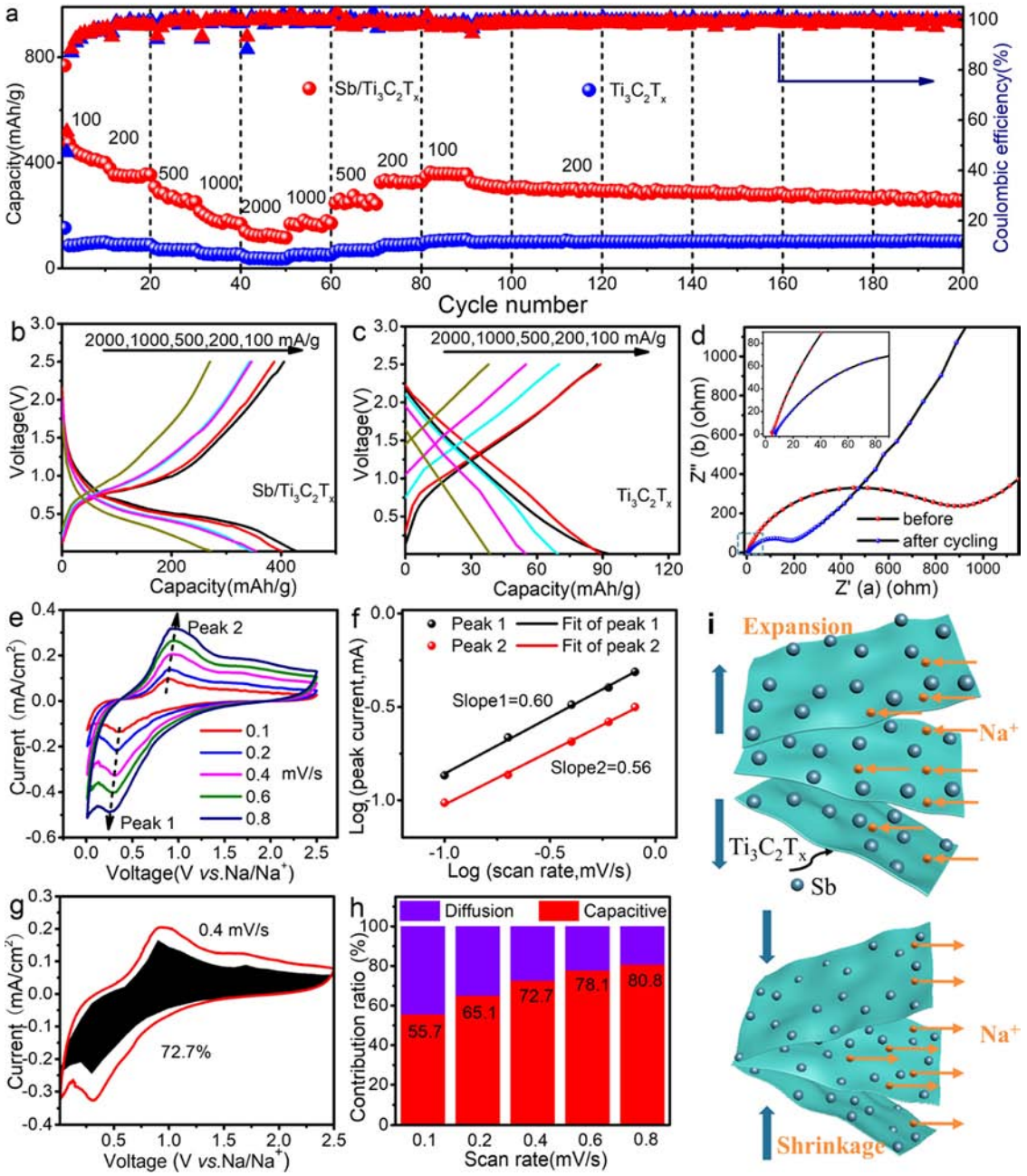


**Figure 5.** (a) Rate performance of $Ti_3C_2T_x$ and Sb/p-$Ti_3C_2T_x$ composites. (b, c) Typical discharge/charge profiles of the samples at various current densities. (d) EIS spectra of Sb/p-$Ti_3C_2T_x$ after cycling at 200 mA $g^{-1}$ for 300 cycles. (e) CV curves at various scan rates. (f) Relationship between log($i$) versus log($v$). (g) Capacitive-controlled contributions at 0.4 mV $s^{-1}$. (h) Normalized ratio of capacitive-controlled and diffusion-controlled contributions. (i) Schematic of expansion and shrinkage for Sb/p-$Ti_3C_2T_x$ during the charge and discharge processes.

reactions to form Na−Sb alloys.[68] Correspondingly, the anodic waves centered at around 0.91 V belong to the stepwise dealloying of Na−Sb alloys.[38] Owing to the ultrasmall particle size of Sb, the phase change during the sodiation/desodiation process is feeble. More distinct information of the electrochemical process can be revealed through the d$Q$/d$V$ curves (Figure 4e), in which two pairs of redox peaks are identified, implying a two-step alloying mechanism.[69] The peak intensity of the following scans greatly reduces in comparison to the first cycle, which results from the amorphization of the sodiation/desodiation product.[70] In addition, the overpotentials of the redox peaks decrease obviously in the subsequent scans due to the rapid activation of the electrode after the initial cycle.[71] Furthermore, the CV profiles nearly overlapped after the first cycle, suggesting the excellent electrochemical stability of the Sb/p-$Ti_3C_2T_x$ electrode.

The cycling stabilities of Sb/p-$Ti_3C_2T_x$ and bare $Ti_3C_2T_x$ are investigated through the constant current charging/discharging test at 50 and 200 mA $g^{-1}$ and displayed in Figure 4d,f, respectively. As the voltage−capacity curves depict in Figure 4b,c, the initial discharge/charge capacities for Sb/p-$Ti_3C_2T_x$ are 722.5/438.1 mAh $g^{-1}$ at 50 mA $g^{-1}$ and 647.1/385.7 mAh $g^{-1}$ at 200 mA $g^{-1}$, corresponding to initial Coulombic efficiencies of 60.6 and 59.6%, respectively. The capacity loss results from the irreversible insertion of $Na^+$ and deposition of the SEI membrane.[67,72] After the initial cycle, the Coulombic


https://doi.org/10.1021/acsaem.1c01863
ACS Appl. Energy Mater. 2021, 4, 9806−9815

efficiency fast climbs above 90%, and the voltage−capacity curves overlap very well in the following cycles, indicating good stability. Furthermore, there is almost no change in the overpotential at 200 mA $g^{-1}$ in contrast to that at 50 mA $g^{-1}$ due to the excellent reaction kinetics of Sb/p-$Ti_3C_2T_x$ composites. Sb/p-$Ti_3C_2T_x$ composites can deliver a stable discharge capacity of 461.3 mAh $g^{-1}$ at 50 mA $g^{-1}$ and maintain 350.6 mAh $g^{-1}$ after 100 cycles, with a capacity retention rate of 76%. A longer cycling test is carried out with a current density of 200 mA $g^{-1}$, as shown in Figure 4f. The Sb composites deliver a stable discharge capacity of 425.1 mAh $g^{-1}$ at 200 mA $g^{-1}$ and retain 216.8 mAh $g^{-1}$ after 300 cycles. In addition, compared with the fresh electrode, a general lamellar structure with well-dispersed nanoparticles can be maintained after cycling (Figure S8), demonstrating the stable structure integrity of the electrode due to chemical bonding between Sb and $Ti_3C_2T_x$.[73] In contrast, although bare $Ti_3C_2T_x$ exhibits superb cycling stability, it delivers comparatively low discharge capacities of around 106 mAh $g^{-1}$ at 50 mA $g^{-1}$ and 66 mAh $g^{-1}$ at 200 mA $g^{-1}$ (Figure 4d,f). For Sb/$Ti_3C_2T_x$ (Figure S9), a specific capacity of 211 mAh $g^{-1}$ can be attained after 150 cycles, showing faster capacity decay due to lack of partial intercalated active Sb. On account of high conductivity, flexibility, and stability, f-$Ti_3C_2T_x$ is demonstrated to be an ideal carrier for Sb nanoparticles to optimize the electrochemical performance of pure Sb electrodes (Figure S10).

Highly conductive $Ti_3C_2T_x$ with an ultrathin flake-like morphology and an enlarged interlayer spacing could boost the rapid insertion and diffusion of $Na^+$ and charge transfer. We also evaluated the rate performance of the electrodes, as shown in Figure 5a. When the rate increases from 100 to 2000 mA $g^{-1}$, the capacity retention rate of bare f-$Ti_3C_2T_x$ reaches 38%. When composited with Sb nanoparticles, the kinetics superiority of f-$Ti_3C_2T_x$ can be fully exerted. The composites deliver capacities of 423.1, 354.1, 274.3, 184.8, and 126.6 mAh $g^{-1}$ at 100, 200, 500, 1000, and 2000 mA $g^{-1}$, respectively. Furthermore, the capacity recovers stepwise with the reduction of current density, generating a complete "V" letter. After the rate test, the electrodes can still work steadily at 200 mA $g^{-1}$, indicating excellent structural stability. The voltage−capacity curves of Sb/p-$Ti_3C_2T_x$ and $Ti_3C_2T_x$ at different rates are displayed in Figure 5b,c, respectively. Even at a high rate of 2 A $g^{-1}$, the electrochemical platform of the Sb/p-$Ti_3C_2T_x$ electrode is obvious and stable with a slight increase of overpotential. In contrast, there is no obvious potential platform in the voltage−capacity curves of bare $Ti_3C_2T_x$, indicating the predominant capacitive sodiation mechanism. As shown in Figure 5d, electrochemical impedance spectroscopy (EIS) measurements are investigated to confirm the charge transfer kinetics of Sb/p-$Ti_3C_2T_x$ composites. The diameter of the semicircle at a high-to-medium frequency region corresponds to the value of charge transfer resistance. Compared with the value of the fresh electrode before cycling, the composites display an obvious decrease in charge transfer impedance, reflecting the effective activation process and better electrochemical contact between the electrode and the electrolyte, together with the enlarged interlayer spacing of flexible $Ti_3C_2T_x$ due to cyclic ion intercalation/deintercalation and volume expansion of partial intercalated Sb.[26,47] The mechanism of sodium storage of Sb/p-$Ti_3C_2T_x$ is further analyzed quantitatively. The contribution ratios of the surface-controlled (capacitive) process and the diffusion-controlled process can be calculated based on the CV curves at different sweep speeds from 0.1 to 0.8 mV $s^{-1}$ (Figure 5e). The peak current ($i$) and sweep speed ($v$) obey the following equation[74]

$$i = av^b (0.5 \leq b \leq 1)$$

where $a$ and $b$ are variable parameters, particularly, the $b$ value reflects the governing factor of the electrochemical sodium storage process. Extremely, $b$ = 0.5 represents the diffusion-controlled process, while $b$ = 1.0 corresponds to the surface-controlled process.[58] On basis of the above equation, the $b$ value can be determined by the slope of $\log(i)$ versus $\log(i)$ curve, as shown in Figure 5f. The linear fitting result reveals the $b$ values of 0.60 and 0.56 for peaks 1 and 2, respectively, indicating that the sodium storage kinetics of Sb/p-$Ti_3C_2T_x$ is both controlled by capacitive- and diffusion-controlled behaviors. The contribution ratios of the capacitive process at various scan rates can be further quantified by the analysis method invented by Dunn et al.[75] The current response at a certain voltage $V$ varies with the scan rate ($v$) and can be expressed by the following equation[76]

$$i(v)|_V = k_1 v + k_2 v^{1/2}$$

where $k_1 v$ and $k_2 v^{1/2}$ represent the current contribution from the surface-controlled process and the diffusion-controlled process, respectively. Hence, the capacitive and diffusive proportions can be figured out by the linear fitting result of $i(v)|_V/v^{1/2}$ versus $v^{1/2}$. As shown in Figure 5g, at a scan rate of 0.4 mV $s^{-1}$, the integral result of the capacitive current response quantitatively separated from the total current response exhibits a high proportion of 72.7%. Significantly, the capacitive contribution ratio improves from 55.7 to 80.8% as the scan rate increases from 0.1 to 0.8 mV $s^{-1}$ (Figure 5h). The high ratios of capacitive contribution are accountable for the superior rate performance of the Sb/p-$Ti_3C_2T_x$ composite, which results from the excellent physicochemical properties, advanced construction, and ingenious cooperation of the components. Especially, as schematically depicted in Figure 5i, the flexible f-$Ti_3C_2T_x$ sheets with the enlarged interlayer spacing enable the highly reversible expansion and shrinkage, which is favorable to the cycling stability and rapid $Na^+$ diffusion kinetics.

Based on the above discussion, ultrafine Sb particles and f-$Ti_3C_2T_x$ nanosheets are an ideal combination. Particularly, the synergistic effect can effectively improve the electrochemical performance of both components, which is graphically depicted in Figure 6. On the one hand, the highly metallic conductive $Ti_3C_2T_x$ nanosheets markedly enhance the electron transfer efficiency, promising rapid charge transfer kinetics of Sb nanoparticles. In addition, the flexible nanosheets with abundant surface groups provide adequate sites to accommodate the Sb particles by forming favorable chemical bonding and drastically buffer the volume expansion during $Na^+$ insertion. On the other hand, the anchored Sb nanoparticles on the surface and interface of $Ti_3C_2T_x$ work as an antirestacking agent to inhibit the aggregation of few-layered nanosheets, ensuring the long-term fast reaction kinetics.

## CONCLUSIONS

In summary, lamellar Sb/p-$Ti_3C_2T_x$ composites where partial active Sb was intercalated at the interlayer and ultrafine Sb nanoparticles were tightly anchored on f-$Ti_3C_2T_x$ by a pillaring process coupled with electrostatic adsorption and annealing. The flexible f-$Ti_3C_2T_x$ matrix fabricated through a modified


https://doi.org/10.1021/acsaem.1c01863
ACS Appl. Energy Mater. 2021, 4, 9806−9815

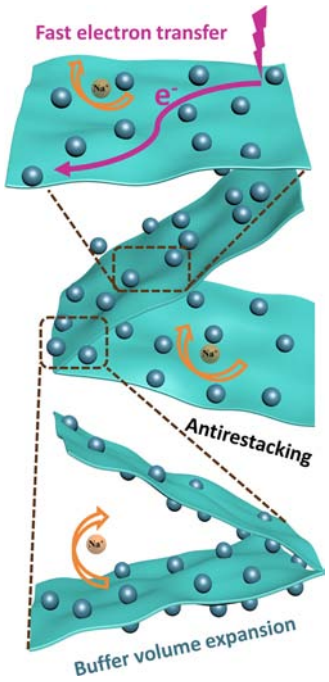


**Figure 6.** Schematic mechanism for the improved performance of Sb/p-$Ti_3C_2T_x$ in SIBs.

solution-phase flocculation approach works as an ideal carrier for Sb nanoparticles by constructing an efficient conductive network and generating strong interfacial interaction, which provides enhanced conductivity and structural stability against particle pulverization and aggregation during incessant $Na^+$ insertion/extraction. Moreover, Sb nanoparticles are evenly distributed on the surface and interface of $Ti_3C_2T_x$, acting as a steric fence to inhibit the agglomeration and collapse of $Ti_3C_2T_x$ nanosheets. The synergistic effect between the f-$Ti_3C_2T_x$ matrix and ultrafine Sb particles is responsible for the excellent electrochemical sodium storage performance with a high retention rate and long cycle stability. Sb/p-$Ti_3C_2T_x$ composites demonstrate the superiority of f-MXenes as a matrix for sodium-ion battery anodes with drastic volume fluctuation and insufficient conductivity. This work further broadens the applications of f-MXenes and provides a feasible strategy to design high-performance pillared MXene-based composites for SIBs, extending the preparation and application of pillared MXene-based composites.

## ■ ASSOCIATED CONTENT

### Supporting Information

The Supporting Information is available free of charge at https://pubs.acs.org/doi/10.1021/acsaem.1c01863.

SEM images of $Ti_3AlC_2$; $Ti_3C_2T_x$ MXenes; characterization of Sb powders; and electrochemical performance of Sb powders (PDF)

## ■ AUTHOR INFORMATION

### Corresponding Author

**Wei-Qiang Han** − *School of Materials Science and Engineering, Zhejiang University, Hangzhou 310027, China;* orcid.org/0000-0001-5525-8277; Email: hanwq@zju.edu.cn

### Authors

**Shunlong Zhang** − *School of Materials Science and Engineering, Zhejiang University, Hangzhou 310027, China;* orcid.org/0000-0003-3872-5085

**Hangjun Ying** − *School of Materials Science and Engineering, Zhejiang University, Hangzhou 310027, China;* orcid.org/0000-0001-9758-4847

**Pengfei Huang** − *School of Materials Science and Engineering, Zhejiang University, Hangzhou 310027, China*

**Jianli Wang** − *School of Materials Science and Engineering, Zhejiang University, Hangzhou 310027, China*

**Zhao Zhang** − *School of Materials Science and Engineering, Zhejiang University, Hangzhou 310027, China*

**Zhihao Zhang** − *School of Materials Science and Engineering, Zhejiang University, Hangzhou 310027, China*

Complete contact information is available at: https://pubs.acs.org/10.1021/acsaem.1c01863

### Author Contributions

[§]S.Z. and H.Y. contributed equally to this work. S.Z. carried out the experiments. H.Y. drafted the manuscript. P.H., J.W., and Z.Z. helped with characterization and discussed the results. W.-Q.H. supervised the entire work. All authors helped with writing the manuscript.

### Notes

The authors declare no competing financial interest.

## ■ ACKNOWLEDGMENTS

This work was supported by the fund from Taihu Electric Corporation 0001, the National Natural Science Foundation of China (51901206), and the Fundamental Research Funds for the Central Universities (2021QNA4003).

## ■ REFERENCES

(1) Naguib, M.; Kurtoglu, M.; Presser, V.; Lu, J.; Niu, J.; Heon, M.; Hultman, L.; Gogotsi, Y.; Barsoum, M. W. Two-Dimensional Nanocrystals Produced by Exfoliation of $Ti_3AlC_2$. *Adv. Mater.* **2011**, *23*, 4248−4253.

(2) Anasori, B.; Lukatskaya, M. R.; Gogotsi, Y. 2D Metal Carbides and Nitrides (MXenes) for Energy Storage. *Nat. Rev. Mater.* **2017**, *2*, No. 16098.

(3) Chaudhari, N. K.; Jin, H.; Kim, B.; San Baek, D.; Joo, S. H.; Lee, K. MXene: an Emerging Two-Dimensional Material for Future Energy Conversion and Storage Applications. *J. Mater. Chem. A* **2017**, *5*, 24564−24579.

(4) Alhabeb, M.; Maleski, K.; Anasori, B.; Lelyukh, P.; Clark, L.; Sin, S.; Gogotsi, Y. Guidelines for Synthesis and Processing of 2D Titanium Carbide ($Ti_3C_2T_x$ MXene). *Chem. Mater.* **2017**, *29*, 7633−7644.

(5) Zhang, S.; Han, W.-Q. Recent Advances in MXenes and Their Composites in Lithium/Sodium Batteries from the Viewpoints of Components and Interlayer Engineering. *Phys. Chem. Chem. Phys.* **2020**, *22*, 16482−16526.

(6) Zheng, W.; Zhang, P.; Chen, J.; Tian, W. B.; Zhang, Y. M.; Sun, Z. M. In situ Synthesis of CNTs@$Ti_3C_2$ Hybrid Structures by Microwave Irradiation for High-Performance Anodes in Lithium Ion Batteries. *J. Mater. Chem. A* **2018**, *6*, 3543−3551.

(7) Nan, J.; Guo, X.; Xiao, J.; Li, X.; Chen, W.; Wu, W.; Liu, H.; Wang, Y.; Wu, M.; Wang, G. Nanoengineering of 2D MXene-Based Materials for Energy Storage Applications. *Small* **2021**, *17*, No. 1902085.

(8) Tang, X.; Guo, X.; Wu, W.; Wang, G. 2D Metal Carbides and Nitrides (MXenes) as High-Performance Electrode Materials for Lithium-Based Batteries. *Adv. Energy Mater.* **2018**, *8*, No. 1801897.

(9) Li, N.; Peng, J.; Ong, W.-J.; Ma, T.; Arramel; Zhang, P.; Jiang, J.; Yuan, X.; Zhang, C. MXenes: An Emerging Platform for Wearable Electronics and Looking Beyond. *Matter* **2021**, *4*, 377−407.
(10) Abdolhosseinzadeh, S.; Jiang, X.; Zhang, H.; Qiu, J.; Zhang, C. Perspectives on solution processing of two-dimensional MXenes *Mater. Today* 2021, DOI: 10.1016/j.mattod.2021.02.010.
(11) Zhang, C. Interfacial Assembly of Two-Dimensional MXenes. *J. Energy Chem.* **2021**, *60*, 417−434.
(12) Abdolhosseinzadeh, S.; Heier, J.; Zhang, C. Coating Porous MXene Films with Tunable Porosity for High-Performance Solid-State Supercapacitors. *ChemElectroChem* **2021**, *8*, 1911−1917.
(13) Zhu, Q.; Li, J.; Simon, P.; Xu, B. Two-Dimensional MXenes for Electrochemical Capacitor Applications: Progress, Challenges and Perspectives. *Energy Storage Mater.* **2021**, *35*, 630−660.
(14) Lipton, J.; Röhr, J. A.; Dang, V.; Goad, A.; Maleski, K.; Lavini, F.; Han, M.; Tsai, E. H. R.; Weng, G.-M.; Kong, J.; Riedo, E.; Gogotsi, Y.; Taylor, A. D. Scalable, Highly Conductive, and Micropatternable MXene Films for Enhanced Electromagnetic Interference Shielding. *Matter* **2020**, *3*, 546−557.
(15) Er, D.; Li, J.; Naguib, M.; Gogotsi, Y.; Shenoy, V. B. $Ti_3C_2$ MXene as a High Capacity Electrode Material for Metal (Li, Na, K, Ca) Ion Batteries. *ACS Appl. Mater. Interfaces* **2014**, *6*, 11173−11179.
(16) Li, Y.; Shao, H.; Lin, Z.; Lu, J.; Liu, L.; Duployer, B.; Persson, P. O. Å.; Eklund, P.; Hultman, L.; Li, M.; Chen, K.; Zha, X.-H.; Du, S.; Rozier, P.; Chai, Z.; Raymundo-Piñero, E.; Taberna, P.-L.; Simon, P.; Huang, Q. A General Lewis Acidic Etching Route for Preparing MXenes with Enhanced Electrochemical Performance in Non-Aqueous Electrolyte. *Nat. Mater.* **2020**, *19*, 894−899.
(17) Li, X.; Li, N.; Huang, Z.; Chen, Z.; Zhao, Y.; Liang, G.; Yang, Q.; Li, M.; Huang, Q.; Dong, B.; Fan, J.; Zhi, C. Confining Aqueous Zn−Br Halide Redox Chemistry by $Ti_3C_2T_X$ MXene. *ACS Nano* **2021**, *15*, 1718−1726.
(18) Sun, Z.; Wang, X.; Zhao, H.; Koh, S. W.; Ge, J.; Zhao, Y.; Gao, P.; Wang, G.; Li, H. Rambutan-Like Hollow Carbon Spheres Decorated with Vacancy-Rich Nickel Oxide for Energy Conversion and Storage. *Carbon Energy* **2020**, *2*, 122−130.
(19) Sun, Z.; Li, K.; Koh, S. W.; Jiao, L. A Green and Simple Method for Energy Storage and Conversion Application. *J. Mater. Sci.* **2021**, *56*, 3354−3363.
(20) Brady, A.; Liang, K.; Vuong, V. Q.; Sacci, R.; Prenger, K.; Thompson, M.; Matsumoto, R.; Cummings, P.; Irle, S.; Wang, H.-W.; Naguib, M. Pre-Sodiated $Ti_3C_2T_x$ MXene Structure and Behavior as Electrode for Sodium-Ion Capacitors. *ACS Nano* **2021**, *15*, 2994−3003.
(21) Bai, Q.; Yang, L.; Chen, H.; Mo, Y. Computational Studies of Electrode Materials in Sodium-Ion Batteries. *Adv. Energy Mater.* **2018**, *8*, No. 1702998.
(22) Song, M.; Tan, H.; Chao, D.; Fan, H. J. Recent Advances in Zn-Ion Batteries. *Adv. Funct. Mater.* **2018**, *28*, No. 1802564.
(23) Fan, M.; Lin, Z.; Zhang, P.; Ma, X.; Wu, K.; Liu, M.; Xiong, X. Synergistic Effect of Nitrogen and Sulfur Dual-Doping Endows $TiO_2$ with Exceptional Sodium Storage Performance. *Adv. Energy Mater.* **2021**, *11*, No. 2003037.
(24) Guo, S.; Feng, Y.; Wang, L.; Jiang, Y.; Yu, Y.; Hu, X. Architectural Engineering Achieves High-Performance Alloying Anodes for Lithium and Sodium Ion Batteries. *Small* **2021**, *17*, No. 2005248.
(25) Luo, J.; Zheng, J.; Nai, J.; Jin, C.; Yuan, H.; Sheng, O.; Liu, Y.; Fang, R.; Zhang, W.; Huang, H.; Gan, Y.; Xia, Y.; Liang, C.; Zhang, J.; Li, W.; Tao, X. Atomic Sulfur Covalently Engineered Interlayers of $Ti_3C_2$ MXene for Ultra-Fast Sodium-Ion Storage by Enhanced Pseudocapacitance. *Adv. Funct. Mater.* **2019**, *29*, No. 1808107.
(26) Xie, X.; Zhao, M.-Q.; Anasori, B.; Maleski, K.; Ren, C. E.; Li, J.; Byles, B. W.; Pomerantseva, E.; Wang, G.; Gogotsi, Y. Porous Heterostructured MXene/Carbon Nanotube Composite Paper with High Volumetric Capacity for Sodium-Based Energy Storage Devices. *Nano Energy* **2016**, *26*, 513−523.
(27) Yu, Y.-X. Prediction of Mobility, Enhanced Storage Capacity, and Volume Change during Sodiation on Interlayer-Expanded Functionalized $Ti_3C_2$ MXene Anode Materials for Sodium-Ion Batteries. *J. Phys. Chem. C* **2016**, *120*, 5288−5296.
(28) Fan, Z.; Wei, C.; Yu, L.; Xia, Z.; Cai, J.; Tian, Z.; Zou, G.; Dou, S. X.; Sun, J. 3D Printing of Porous Nitrogen-Doped $Ti_3C_2$ MXene Scaffolds for High-Performance Sodium-Ion Hybrid Capacitors. *ACS Nano* **2020**, *14*, 867−876.
(29) Zhang, P.; Soomro, R. A.; Guan, Z.; Sun, N.; Xu, B. 3D Carbon-Coated MXene Architectures with High and Ultrafast Lithium/Sodium-Ion Storage. *Energy Storage Mater.* **2020**, *29*, 163−171.
(30) Lim, K. R. G.; Handoko, A. D.; Nemani, S. K.; Wyatt, B.; Jiang, H.-Y.; Tang, J.; Anasori, B.; Seh, Z. W. Rational Design of Two-Dimensional Transition Metal Carbide/Nitride (MXene) Hybrids and Nanocomposites for Catalytic Energy Storage and Conversion. *ACS Nano* **2020**, *14*, 10834−10864.
(31) Zhao, R.; Qian, Z.; Liu, Z.; Zhao, D.; Hui, X.; Jiang, G.; Wang, C.; Yin, L. Molecular-Level Heterostructures Assembled from Layered Black Phosphorene and $Ti_3C_2$ MXene as Superior Anodes for High-Performance Sodium Ion Batteries. *Nano Energy* **2019**, *65*, No. 104037.
(32) Zhao, D.; Zhao, R.; Dong, S.; Miao, X.; Zhang, Z.; Wang, C.; Yin, L. Alkali-Induced 3D Crinkled Porous $Ti_3C_2$ MXene Architectures Coupled with NiCoP Bimetallic Phosphide Nanoparticles as Anodes for High-Performance Sodium-Ion Batteries. *Energy Environ. Sci.* **2019**, *12*, 2422−2432.
(33) Guo, X.; Zhang, W.; Zhang, J.; Zhou, D.; Tang, X.; Xu, X.; Li, B.; Liu, H.; Wang, G. Boosting Sodium Storage in Two-Dimensional Phosphorene/$Ti_3C_2T_x$ MXene Nanoarchitectures with Stable Fluorinated Interphase. *ACS Nano* **2020**, *14*, 3651−3659.
(34) Zhang, H.; Qi, Q.; Zhang, P.; Zheng, W.; Chen, J.; Zhou, A.; Tian, W.; Zhang, W.; Sun, Z. Self-Assembled 3D $MnO_2$ Nanosheets@ Delaminated-$Ti_3C_2$ Aerogel as Sulfur Host for Lithium−Sulfur Battery Cathodes. *ACS Appl. Energy Mater.* **2019**, *2*, 705−714.
(35) Wu, Y.; Nie, P.; Wang, J.; Dou, H.; Zhang, X. Few-Layer MXenes Delaminated via High-Energy Mechanical Milling for Enhanced Sodium-Ion Batteries Performance. *ACS Appl. Mater. Interfaces* **2017**, *9*, 39610.
(36) Dong, Y.; Wu, Z.-S.; Zheng, S.; Wang, X.; Qin, J.; Wang, S.; Shi, X.; Bao, X. $Ti_3C_2$ MXene-Derived Sodium/Potassium Titanate Nanoribbons for High-Performance Sodium/Potassium Ion Batteries with Enhanced Capacities. *ACS Nano* **2017**, *11*, 4792−4800.
(37) Dong, Y.; Shi, H.; Wu, Z.-S. Recent Advances and Promise of MXene-Based Nanostructures for High-Performance Metal Ion Batteries. *Adv. Funct. Mater.* **2020**, *30*, No. 2000706.
(38) Liu, Y.; Zhou, B.; Liu, S.; Ma, Q.; Zhang, W.-H. Galvanic Replacement Synthesis of Highly Uniform Sb Nanotubes: Reaction Mechanism and Enhanced Sodium Storage Performance. *ACS Nano* **2019**, *13*, 5885−5892.
(39) Gao, H.; Guo, X.; Wang, S.; Zhang, F.; Liu, H.; Wang, G. Antimony-Based Nanomaterials for High-Performance Potassium-Ion Batteries. *EcoMat* **2020**, *2*, No. e12027.
(40) Luo, J.; Matios, E.; Wang, H.; Tao, X.; Li, W. Interfacial Structure Design of MXene-Based Nanomaterials for Electrochemical Energy Storage and Conversion. *InfoMat* **2020**, *2*, 1057−1076.
(41) Carey, M.; Hinton, Z.; Natu, V.; Pai, R.; Sokol, M.; Alvarez, N. J.; Kalra, V.; Barsoum, M. W. Dispersion and Stabilization of Alkylated 2D MXene in Nonpolar Solvents and Their Pseudocapacitive Behavior. *Cell Rep. Phys. Sci.* **2020**, *1*, No. 100042.
(42) Ghidiu, M.; Halim, J.; Kota, S.; Bish, D.; Gogotsi, Y.; Barsoum, M. W. Ion-Exchange and Cation Solvation Reactions in $Ti_3C_2$ MXene. *Chem. Mater.* **2016**, *28*, 3507−3514.
(43) Zhao, Y.; Wang, L. P.; Sougrati, M. T.; Feng, Z.; Leconte, Y.; Fisher, A.; Srinivasan, M.; Xu, Z. A Review on Design Strategies for Carbon Based Metal Oxides and Sulfides Nanocomposites for High Performance Li and Na Ion Battery Anodes. *Adv. Energy Mater.* **2017**, *7*, No. 1601424.
(44) Xu, M.; Lei, S.; Qi, J.; Dou, Q.; Liu, L.; Lu, Y.; Huang, Q.; Shi, S.; Yan, X. Opening Magnesium Storage Capability of Two-

Dimensional MXene by Intercalation of Cationic Surfactant. *ACS Nano* **2018**, *12*, 3733−3740.
(45) Zhang, S.; Ying, H.; Huang, P.; Wang, J.; Zhang, Z.; Yang, T.; Han, W.-Q. Rational Design of Pillared SnS/$Ti_3C_2T_x$ MXene for Superior Lithium-Ion Storage. *ACS Nano* **2020**, *14*, 17665−17674.
(46) Zhang, S.; Huang, P.; Wang, J.; Zhuang, Z.; Zhang, Z.; Han, W.-Q. Fast and Universal Solution-Phase Flocculation Strategy for Scalable Synthesis of Various Few-Layered MXene Powders. *J. Phys. Chem. Lett.* **2020**, *11*, 1247−1254.
(47) Zhang, S.; Ying, H.; Yuan, B.; Hu, R.; Han, W.-Q. Partial Atomic Tin Nanocomplex Pillared Few-Layered $Ti_3C_2T_x$ MXenes for Superior Lithium-Ion Storage. *Nano-Micro Lett.* **2020**, *12*, No. 78.
(48) Zhang, S.; Ying, H.; Guo, R.; Yang, W.; Han, W.-Q. Vapor Deposition Red Phosphorus to Prepare Nitrogen-Doped $Ti_3C_2T_x$ MXenes Composites for Lithium-Ion Batteries. *J. Phys. Chem. Lett.* **2019**, *10*, 6446−6454.
(49) Zhang, C.; Ma, Y.; Zhang, X.; Abdolhosseinzadeh, S.; Sheng, H.; Lan, W.; Pakdel, A.; Heier, J.; Nüesch, F. Two-Dimensional Transition Metal Carbides and Nitrides (MXenes): Synthesis, Properties, and Electrochemical Energy Storage Applications. *Energy Environ. Mater.* **2020**, *3*, 29−55.
(50) Li, J.; Wang, H.; Xiao, X. Intercalation in Two-Dimensional Transition Metal Carbides and Nitrides (MXenes) toward Electrochemical Capacitor and Beyond. *Energy Environ. Mater.* **2020**, *3*, 306−322.
(51) Shui, W.; Li, J.; Wang, H.; Xing, Y.; Li, Y.; Yang, Q.; Xiao, X.; Wen, Q.; Zhang, H. $Ti_3C_2T_x$ MXene Sponge Composite as Broadband Terahertz Absorber. *Adv. Opt. Mater.* **2020**, *8*, No. 2001120.
(52) Tang, H.; Li, W.; Pan, L.; Tu, K.; Du, F.; Qiu, T.; Yang, J.; Cullen, C. P.; McEvoy, N.; Zhang, C. A Robust, Freestanding MXene-Sulfur Conductive Paper for Long-Lifetime Li−S Batteries. *Adv. Funct. Mater.* **2019**, *29*, No. 1901907.
(53) Luo, J.; Tao, X.; Zhang, J.; Xia, Y.; Huang, H.; Zhang, L.; Gan, Y.; Liang, C.; Zhang, W. $Sn^{4+}$ Ion Decorated Highly Conductive $Ti_3C_2$ MXene: Promising Lithium-Ion Anodes with Enhanced Volumetric Capacity and Cyclic Performance. *ACS Nano* **2016**, *10*, 2491−2499.
(54) Zhang, Q.; Lai, H.; Fan, R.; Ji, P.; Fu, X.; Li, H. High Concentration of $Ti_3C_2T_x$ MXene in Organic Solvent. *ACS Nano* **2021**, *15*, 5249−5262.
(55) Luo, J.; Zhang, W.; Yuan, H.; Jin, C.; Zhang, L.; Huang, H.; Liang, C.; Xia, Y.; Zhang, J.; Gan, Y.; Tao, X. Pillared Structure Design of MXene with Ultralarge Interlayer Spacing for High-Performance Lithium-Ion Capacitors. *ACS Nano* **2017**, *11*, 2459−2469.
(56) Zou, Z.; Wang, Q.; Yan, J.; Zhu, K.; Ye, K.; Wang, G.; Cao, D. Versatile Interfacial Self-Assembly of $Ti_3C_2T_x$ MXene Based Composites with Enhanced Kinetics for Superior Lithium and Sodium Storage. *ACS Nano* **2021**, *15*, 12140−12150.
(57) Nanaji, K.; Upadhyayula, V.; Rao, T. N.; Anandan, S. Robust, Environmentally Benign Synthesis of Nanoporous Graphene Sheets from Biowaste for Ultrafast Supercapacitor Application. *ACS Sustainable Chem. Eng.* **2019**, *7*, 2516−2529.
(58) Zhao, R.; Di, H.; Wang, C.; Hui, X.; Zhao, D.; Wang, R.; Zhang, L.; Yin, L. Encapsulating Ultrafine Sb Nanoparticles in $Na^+$ Pre-Intercalated 3D Porous $Ti_3C_2T_x$ MXene Nanostructures for Enhanced Potassium Storage Performance. *ACS Nano* **2020**, *14*, 13938−13951.
(59) Wang, P.; Lu, X.; Boyjoo, Y.; Wei, X.; Zhang, Y.; Guo, D.; Sun, S.; Liu, J. Pillar-Free $TiO_2/Ti_3C_2$ Composite with Expanded Interlayer Spacing for High-Capacity Sodium Ion Batteries. *J. Power Sources* **2020**, *451*, No. 227756.
(60) Yang, K.; Tang, J.; Liu, Y.; Kong, M.; Zhou, B.; Shang, Y.; Zhang, W.-H. Controllable Synthesis of Peapod-like Sb@C and Corn-like C@Sb Nanotubes for Sodium Storage. *ACS Nano* **2020**, *14*, 5728−5737.
(61) Wan, F.; Guo, J.-Z.; Zhang, X.-H.; Zhang, J.-P.; Sun, H.-Z.; Yan, Q.; Han, D.-X.; Niu, L.; Wu, X.-L. In Situ Binding Sb Nanospheres on Graphene via Oxygen Bonds as Superior Anode for Ultrafast Sodium-Ion Batteries. *ACS Appl. Mater. Interfaces* **2016**, *8*, 7790−7799.
(62) Fang, Y.; Zhang, Y.; Zhu, K.; Lian, R.; Gao, Y.; Yin, J.; Ye, K.; Cheng, K.; Yan, J.; Wang, G.; Wei, Y.; Cao, D. Lithiophilic Three-Dimensional Porous $Ti_3C_2T_x$-rGO Membrane as a Stable Scaffold for Safe Alkali Metal (Li or Na) Anodes. *ACS Nano* **2019**, *13*, 14319−14328.
(63) Yang, X.; Wang, Q.; Zhu, K.; Ye, K.; Wang, G. L.; Cao, D. X.; Yan, J. 3D Porous Oxidation-Resistant MXene/Graphene Architectures Induced by In Situ Zinc Template toward High-Performance Supercapacitors. *Adv. Funct. Mater.* **2021**, *31*, No. 2101087.
(64) Zhou, G.; Wang, D.-W.; Yin, L.-C.; Li, N.; Li, F.; Cheng, H.-M. Oxygen Bridges between NiO Nanosheets and Graphene for Improvement of Lithium Storage. *ACS Nano* **2012**, *6*, 3214−3223.
(65) Wang, M.; Yang, Z.; Wang, J.; Li, W.; Gu, L.; Yu, Y. Sb Nanoparticles Encapsulated in a Reticular Amorphous Carbon Network for Enhanced Sodium Storage. *Small* **2015**, *11*, 5381−5387.
(66) Xu, A.; Xia, Q.; Zhang, S.; Duan, H.; Yan, Y.; Wu, S. Ultrahigh Rate Performance of Hollow Antimony Nanoparticles Impregnated in Open Carbon Boxes for Sodium-Ion Battery under Elevated Temperature. *Small* **2019**, *15*, No. 1903521.
(67) Kong, M.; Liu, Y.; Zhou, B.; Yang, K.; Tang, J.; Zhang, P.; Zhang, W.-H. Rational Design of Sb@C@TiO2 Triple-Shell Nanoboxes for High-Performance Sodium-Ion Batteries. *Small* **2020**, *16*, No. 2001976.
(68) Yang, J.; Li, J.; Wang, T.; Notten, P. H. L.; Ma, H.; Liu, Z.; Wang, C.; Wang, G. Novel Hybrid of Amorphous Sb/N-Doped Layered Carbon for High-Performance Sodium-Ion Batteries. *Chem. Eng. J.* **2021**, *407*, No. 127169.
(69) Qian, J.; Chen, Y.; Wu, L.; Cao, Y.; Ai, X.; Yang, H. High Capacity Na-storage and Superior Cyclability of nanocomposite Sb/C anode for Na-ion batteries. *Chem. Commun.* **2012**, *48*, 7070−7072.
(70) Subramanyan, K.; Aravindan, V. Stibium: A Promising Electrode toward Building High-Performance Na-Ion Full-Cells. *Chem* **2019**, *5*, 3096−3126.
(71) Wang, J.; Yan, X.; Zhang, Z.; Ying, H.; Guo, R.; Yang, W.; Han, W.-Q. Facile Preparation of High-Content N-Doped CNT Microspheres for High-Performance Lithium Storage. *Adv. Funct. Mater.* **2019**, *29*, No. 1904819.
(72) Chen, H.; Chen, N.; Zhang, M.; Li, M.; Gao, Y.; Wang, C.; Chen, G.; Du, F. $Ti_3C_2T_x$ MXene Decorated With Sb Nanoparticles as Anodes Material for Sodium-Ion Batteries. *Nanotechnology* **2019**, *30*, No. 134001.
(73) Ren, M.; Cao, D.; Jiang, W.; Su, K.; Pan, L.; Jiang, Y.; Yan, S.; Qiu, T.; Yang, M.; Yang, J.; Zhang, C. Hierarchical Composite of $Sb_2S_3$ decorated on highly crumpled $Ti_3C_2T_x$ nanosheets for enhanced sodium storage properties. *Electrochim. Acta* **2021**, *373*, No. 137835.
(74) Meng, R.; Huang, J.; Feng, Y.; Zu, L.; Peng, C.; Zheng, L.; Zheng, L.; Chen, Z.; Liu, G.; Chen, B.; Mi, Y.; Yang, J. Black Phosphorus Quantum Dot/$Ti_3C_2$ MXene Nanosheet Composites for Efficient Electrochemical Lithium/Sodium-Ion Storage. *Adv. Energy Mater.* **2018**, *8*, No. 1801514.
(75) Augustyn, V.; Come, J.; Lowe, M. A.; Kim, J. W.; Taberna, P.-L.; Tolbert, S. H.; Abruña, H. D.; Simon, P.; Dunn, B. High-Rate Electrochemical Energy Storage Through $Li^+$ Intercalation Pseudocapacitance. *Nat. Mater.* **2013**, *12*, 518−522.
(76) Zhao, R.; Di, H.; Hui, X.; Zhao, D.; Wang, R.; Wang, C.; Yin, L. Self-Assembled $Ti_3C_2$ MXene and N-Rich Porous Carbon Hybrids as Superior Anodes for High-Performance Potassium-Ion Batteries. *Energy Environ. Sci.* **2020**, *13*, 246−257.


https://doi.org/10.1021/acsaem.1c01863
*ACS Appl. Energy Mater.* 2021, 4, 9806−9815